



# Nemo-Nordic 2.0: Operational marine forecast model for the Baltic Sea

Tuomas Kärnä<sup>1</sup>, Patrik Ljungemyr<sup>2</sup>, Saeed Falahat<sup>2</sup>, Ida Ringgaard<sup>3</sup>, Lars Axell<sup>2</sup>, Vasily Korabel<sup>3</sup>, Jens Murawski<sup>3</sup>, Ilja Maljutenko<sup>4</sup>, Anja Lindenthal<sup>5</sup>, Simon Jandt-Scheelke<sup>5</sup>, Svetlana Verjovkina<sup>4</sup>, Ina Lorkowski<sup>5</sup>, Priidik Lagemaa<sup>4</sup>, Jun She<sup>3</sup>, Laura Tuomi<sup>1</sup>, Adam Nord<sup>2</sup>, and Vibeke Huess<sup>3</sup>

<sup>1</sup>Finnish Meteorological Institute, Helsinki, Finland

<sup>2</sup>Swedish Meteorological and Hydrological Institute, Norrköping, Sweden

<sup>3</sup>Danish Meteorological Institute, Copenhagen, Denmark

<sup>4</sup>Tallinn University of Technology, Tallinn, Estonia

<sup>5</sup>Bundesamt für Seeschifffahrt und Hydrographie, Hamburg, Germany

**Correspondence:** Tuomas Kärnä (tuomas.karna@fmi.fi)

1 **Abstract.** This paper describes Nemo-Nordic 2.0, an operational marine forecast model for the Baltic Sea. The model is  
2 based on the NEMO (Nucleus for European Modelling of the Ocean) circulation model and the previous Nemo-Nordic 1.0  
3 configuration by Hordoir et al. [Geosci. Model Dev., 12, 363–386, 2019]. The most notable updates include the switch from  
4 NEMO version 3.6 to 4.0, updated model bathymetry and revised bottom friction formulation. The model domain covers the  
5 Baltic and the North Seas with approximately 1 nautical mile resolution. Vertical grid resolution has been increased from 3 to  
6 1 m in the surface layer. In addition, the numerical solver configuration has been revised to reduce artificial mixing to improve  
7 the representation of inflow events. Sea-ice is modeled with the SI3 model instead of LIM3. The model is validated against  
8 sea level, water temperature and salinity observations, as well as Baltic Sea ice chart data for a two-year hindcast simulation.  
9 Sea level root mean square deviation (RMSD) is typically within 10 cm throughout the Baltic basin. Seasonal sea surface  
10 temperature variation is well captured, although the model exhibits a negative bias of approximately  $-0.5^{\circ}\text{C}$ . Salinity RMSD is  
11 typically below 1.5 g/kg. The model captures the 2014 Major Baltic Inflow event and its propagation to the Gotland Deep. The  
12 skill analysis demonstrates that Nemo-Nordic 2.0 can reproduce the hydrographic features of the Baltic Sea.

## 13 1 Introduction

14 The Baltic Sea is a brackish, semi-enclosed water body in the northern Europe (Figure 1). It has unique characteristics due to  
15 large freshwater input and restricted water exchange with the North Sea. The circulation in the Baltic basin has been simulated  
16 with several numerical models with varying configurations (e.g., Lehmann, 1995; Meier et al., 1999; Funkquist and Kleine,  
17 2007; Berg and Poulsen, 2012; Gräwe et al., 2015a; Hordoir et al., 2019). Due to the complex non-linear interaction with the  
18 North Sea (Gustafsson, 1997; Gustafsson and Andersson, 2001), it is widely accepted that the North and Baltic Seas must be  
19 modeled as a single, coupled system (Daewel and Schrum, 2013; Pätsch et al., 2017; Hordoir et al., 2019).

20 The North Sea is a marginal sea with open connections to the North Atlantic, and hence it is strongly influenced by tides  
21 and influx of Atlantic water (Huthnance, 1991). Tides are predominantly semidiurnal and propagate cyclonically around the



22 North Sea; they dissipate in Kattegat. The northern part of the North Sea is stratified throughout the year due to the outflow  
23 of brackish Baltic water (forming the Norwegian Coastal Current) and inflow of Atlantic water through the deep Norwegian  
24 Trench (Winther and Johannessen, 2006).

25 The shallow Danish Straits region (Fig. 1c) is a transition region between the saline North Sea and the brackish Baltic Sea. In  
26 the Baltic Sea, tides are small ( $< 10$  cm) and play a minor role in sea surface height (SSH) dynamics. Short-term SSH variations  
27 are induced by meteorological forcing: atmospherically-induced seiche oscillations are common and can result in large SSH  
28 variations. In addition, SSH is affected by the total water amount in the Baltic Sea, controlled by the riverine freshwater input  
29 and water exchange through the Danish Straits.

30 In the Baltic Sea, seasonal thermocline starts to develop in late spring and reaches its maximum depth of 10–30 m typically  
31 in late July or early August. The deeper areas of the southern Baltic Sea, Baltic Proper and Gulf of Finland have permanent  
32 stratification, the halocline lying typically at 40–80 m depth. The Gulf of Bothnia, on the other hand, has a relatively weak  
33 salinity stratification: Seasonal mixing reaches depths of 80–90 m and permanent stratification exists only in the deeper parts  
34 of the Bothnian Sea.

35 During the winter, sea surface temperature (SST) reaches the freezing point in the northern parts of the Baltic Sea and sea  
36 ice forms every year. During average winters, about 45% of the surface area freezes; In severe winters the entire Baltic Sea can  
37 be covered by sea ice (Leppäranta and Myrberg, 2009).

38 The salt balance in the Baltic Sea is controlled by freshwater discharge, vertical mixing, and episodic salt water inflows  
39 through the Danish Straits. The Major Baltic Inflow (MBI) events bring large quantities of saline water into the Baltic Sea.  
40 Large MBIs occur roughly once per decade (Mohrholz, 2018) and are important for maintaining the salt balance as well as  
41 ventilating the oxygen-depleted deep waters in the Baltic Sea (Mohrholz et al., 2015; Gräwe et al., 2015b). MBIs are driven  
42 by barotropic pressure gradient (sea level difference) between Kattegat and the Arkona basin. The barotropic forcing brings  
43 saline water from Kattegat into the Arkona basin (Gustafsson and Andersson, 2001). From there onward the inflow continues  
44 as a baroclinic bottom current filling the subsequent sub-basins (Gräwe et al., 2015b).

45 Saline waters can enter the Arkona basin via two routes: Via the Belt Sea, or through the Sound (Fig. 1c). The main inflow  
46 pathway is through the Great Belt and subsequently the Belt Sea; The final obstruction in this route is the Darss Sill where water  
47 depth is 18 m. The secondary, faster route is via the Sound, separated from the Arkona basin by the Drogden Sill (8 m sill  
48 depth). The volume flux through the Belt Sea is significantly higher (typically 70% – 80% of total volume flux; Mohrholz et al.  
49 2015).

50 Modeling the circulation in the Baltic Sea is challenging due to the complex topography, strong stratification, and dense  
51 inflows related to the MBIs. Water exchange in the system is governed by the fluxes between the sub-basins. Many constraining  
52 regions, such as the Danish Straits or the Archipelago Sea, are characterized by fine-scale bathymetric features that are difficult  
53 to resolve in operational models. Representing the Danish Straits region, for example, requires sub-kilometer scale horizontal  
54 resolution (She et al., 2007; Gräwe et al., 2015a; Stanev et al., 2018). Similarly, the Archipelago Sea consists of narrow channels  
55 and thousands of small islands that cannot be captured with typical grid resolutions. In practice, resolving the dynamics in these  
56 regions requires nested grids (Gräwe et al., 2015a) or unstructured meshes (Stanev et al., 2018).



57 Salt pulses propagate as a density-driven bottom current from basin to basin. In circulation models, artificial numerical  
58 mixing can slow down or completely arrest the propagation of the current; Numerical mixing dilutes the water masses, reducing  
59 the horizontal pressure gradient as well as stratification. Spurious vertical mixing can also erode the permanent halocline in  
60 deeper basins, leading into excessive ventilation of the oxygen-depleted deep waters. In finite volume models, the accuracy  
61 of the advection scheme has a significant impact on the level of numerical mixing Zalesak (1979); Hourdin and Armengaud  
62 (1999); Lévy et al. (2001). Previous studies suggest that vertical grid resolution plays an important role in retaining the salt  
63 pulse density structure in the Baltic Sea (Hofmeister et al., 2011; Gräwe et al., 2015a).

64 Operational ocean modeling has a fairly long history in the Baltic Sea, starting already in the mid 1990s with HIROMB (High  
65 Resolution Operational Model for the Baltic). It was a cooperation involving many Baltic institutes who gathered around a  
66 common circulation model with the same name. The cooperation itself later became the modeling part of the Baltic Operational  
67 Oceanographic System (BOOS; <https://boos.org>; She et al. 2020), or the BOOS Modelling Programme. The HIROMB model  
68 itself existed in several branches in different institutes for many years, e.g. the HIROMB model (Funkquist and Kleine, 2007;  
69 Axell, 2013) at the Swedish Meteorological and Hydrological Institute (SMHI), and the HIROMB BOOS Model (HBM; Berg  
70 and Poulsen 2012). The first version of a common circulation model built around the Nucleus for European Modelling of the  
71 Ocean (NEMO) was called Nemo-Nordic 1.0 and was described and validated by Pemberton et al. (2017) and Hordoir et al.  
72 (2019). It was based on NEMO version 3.6 and was coupled to the integrated ice model LIM3 (Vancoppenolle et al., 2009).

73 In this paper, we present an updated Nemo-Nordic 2.0 operational forecast system for the Baltic Sea based on the NEMO  
74 circulation model version 4.0 (Madec et al. 2019). The model domain covers the North and Baltic Seas (Fig. 1). The setup is  
75 based on the Nemo-Nordic 1.0 configuration (Hordoir et al., 2019). Compared to Nemo-Nordic 1.0, most notable updates are  
76 the switch from NEMO 3.6 to NEMO 4.0, updated bathymetry and revised bottom friction formulation. Vertical grid resolution  
77 has been increased in the surface layer from 3 to 1 m. We have also revised the numerical schemes (e.g. advection of momentum  
78 and tracers) to reduce artificial mixing. Finally, NEMO 4.0 uses the SI3 sea ice model instead of LIM3.

79 The aim of this article is to validate the operational Nemo-Nordic 2.0 forecast system. The model configuration is identical  
80 to the operational EU Copernicus Marine Service forecast model for the Baltic Sea. The validation is based on a 2-year  
81 hindcast simulation that uses similar forcing as in the operational configuration. The presented validation run uses a 3 km DMI  
82 HIRLAM atmospheric forcing whereas the operational model will use 2.5 km MetCoOP HARMONIE model forecast padded  
83 with ECMWF HRES forecast data in North Sea regions outside the MetCoOP domain.

84 The Nemo-Nordic 2.0 model skill is assessed with respect to SSH, water temperature and salinity, as well as sea ice coverage  
85 using observations from tide gauges, FerryBox instruments, vertical profiles, as well as ice charts. The model configuration  
86 and used observation data sets are presented in Section 2. Section 3 presents the model skill metrics, followed by a discussion  
87 and conclusions in Section 4.

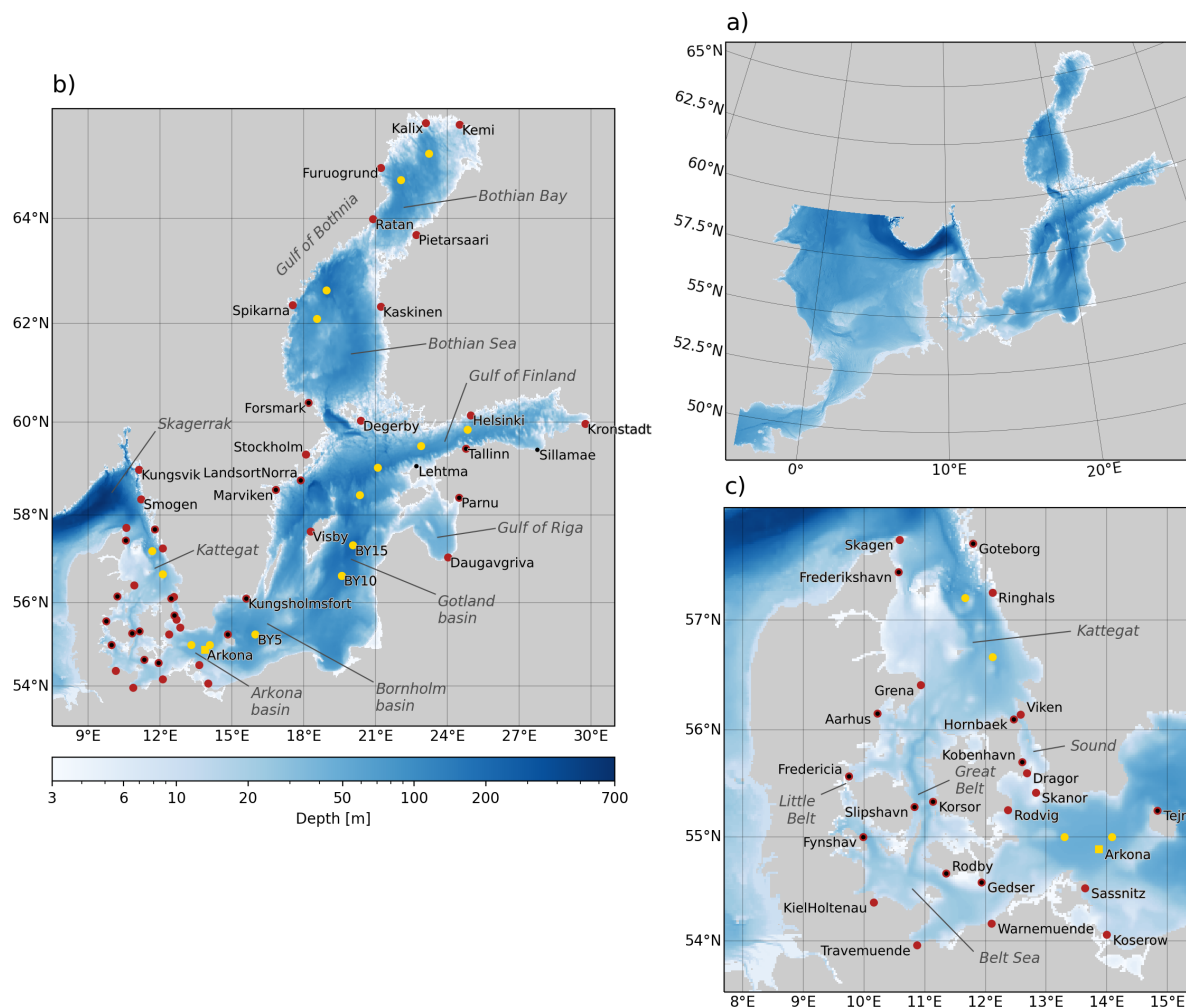


**Figure 1.** Computational domain and bathymetry; a) the entire model domain, b) the Baltic Sea, c) Danish Straits region. Red and black dots indicate station locations with SSH and SST observations, respectively; Yellow dots indicate vertical profile locations.

## 88 2 Methods

### 89 2.1 Model domain and configuration

90 The model setup is based on the Nemo-Nordic 1.0 configuration (Hordoir et al., 2019) and NEMO version 4.0 (Madedc  
91 et al. 2019; subversion repository revision 11281). The grid covers the North and Baltic Seas, spanning from 4.15278°W  
92 to 30.18021°E and 48.4917°N to 65.8914216°N (Figure 1 a). The grid spacing is 0.0277775° and 0.0166664° in the zonal and  
93 meridional directions, respectively, resulting in approximately 1 nautical mile resolution. In the North Sea, the open boundaries  
94 are located in the western part of the English Channel and between Scotland and Norway.



95 The model uses a  $z^*$  grid in the vertical direction, consisting of 56 levels. The layer thickness is 1 m at the surface, increasing  
96 to 10 m at 75 m depth, and maximum 24 m at 700 m depth. In the bottom cell a partial step formulation is used, i.e. the location  
97 of the bottom node is fitted to the local bathymetry instead of fixing it to the full  $z$  level height.

98 The model's bathymetry is derived from the global GEBCO data set (the GEBCO-2014 grid, version 20150318; <http://www.gebco.net>, last access: March 29, 2021). The data was interpolated to the centroids of the model grid. The land mask was  
99 generated from OpenStreetMap coastline data (<https://www.openstreetmap.org>, last access: March 29, 2021) and the GEBCO  
100 bathymetry. In the Baltic Sea, the minimum depth was set to 3 m. In the North Sea, the minimum depth varies between 5 and  
101 10 m to accommodate tidal variations as wetting and drying is not taken into account. The bathymetry was modified along  
102 the west coast of Denmark by masking out shallow regions (such as the Limfjord area) to improve the propagation of tides to  
103 Skagerrak and Kattegat. Furthermore, to improve the inflow of salt water into the Baltic Sea, the bathymetry was modified in  
104 the Danish Straits region (see Sect. 2.2).

106 The model configuration was tuned to accurately simulate surface gravity waves and internal gravitational currents. We use  
107 a non-linear free surface formulation with mode-splitting. The baroclinic and barotropic time steps are 90 and 3 s, respectively.  
108 Fast variations in the 2D fields are filtered out by averaging over two baroclinic time steps. A vector-invariant form of the mo-  
109 mentum equation is used with an energy and enstrophy conserving advection scheme. This choice improves the representation  
110 of baroclinic eddies, reduces noise in the velocity field and also improves the interaction of currents and topography in partial  
111 step configurations (Madec et al., 2019).

112 Bottom friction is imposed with implicit nonlinear log-layer parameterization. The bottom drag,  $C_d$ , was computed from a  
113 spatially variable bottom roughness length parameter,  $z_0^b$ ,

$$114 \quad C_d = \left( \frac{\kappa}{\log\left(\frac{z_0^b + h_0/2}{z_0^b}\right)} \right)^2, \quad (1)$$

115 where  $h_0$  is height of the bottom cell, and  $\kappa$  is the von Karman constant. As NEMO 4.0 only allows users to specify the  $C_d$  field  
116 directly, the formulation (1) was implemented in NEMO, introducing a user-defined  $z_0^b$  field. With the  $z^*$  vertical coordinates,  
117 the cell height varies in time, and consequently  $C_d$  becomes time dependent. The bottom roughness length formulation (1)  
118 is consistent with the law of the wall boundary layer theory, and it is the preferred parameterization especially in coastal and  
119 shallow regions. The additional benefit is that, unlike  $C_d$ ,  $z_0^b$  does not depend on the cell height, making the configuration more  
120 robust with respect to changes in the vertical grid and bathymetry.

121 The bottom roughness field was tuned to improve sea level skill throughout the model domain. In the English Channel  $z_0^b$   
122 was set to 0.3 mm to avoid dampening the tidal signal along the continental coast. In the northwestern part of the North Sea  
123  $z_0^b = 1$  cm and  $z_0^b = 3$  cm in the Danish Straits to introduce sufficient dissipation. In the Baltic Sea, 1 mm was used to prevent  
124 excessive damping of seiche motions.

125 Vertical turbulence is modeled with the Generic Length Scale model (Umlauf and Burchard, 2003; Reffray et al., 2015),  
126 using  $k - \varepsilon$  closure and Canuto A stability functions. Horizontal diffusion of momentum and tracers were modeled with a  
127 Laplacian formulation with constant-in-time diffusivity and viscosity. In the surface layer (top 10 m), viscosity and diffusivity



128 were set to 50 and  $5 \text{ m}^2 \text{ s}^{-1}$ , respectively. For the rest of the water column, horizontal viscosity was  $0.01 \text{ m}^2 \text{ s}^{-1}$  and diffusivity  
129 was neglected to avoid excessive mixing in the bottom layer (Hordoir et al., 2019).

130 Sea-ice dynamics are modeled with the SI3 sea-ice model. SI3 solves the sea-ice thermodynamics, advection, rheology and  
131 ridging/rafting. The landfast ice parametrization by Lemieux et al. (2016) is used. The model consist of five ice categories and  
132 one snow category. Ice thickness categories are defined with the thickness bounds 0.45, 1.13, 2.14, and 3.67 m. In this work,  
133 we use the standard settings in the sea-ice model, originally developed for the global ocean, for the ice thickness categories;  
134 Further tuning of the configuration for the Baltic Sea will be performed at a later stage.

135 In NEMO 4.0, we use the TEOS-10 equation of state (IOC, 2010; Roquet et al., 2015) to compute water density. Conse-  
136 quently, the modeled water salinity and temperature are in Absolute Salinity (g/kg) and Conservative Temperature ( $^{\circ}\text{C}$ ) units,  
137 respectively. When comparing against observations, the model's temperature is converted to in-situ temperature.

## 138 2.2 Improving salinity inflows

139 Salt water inflows to the Baltic Sea are extremely sensitive to bathymetric features, especially in the Danish Straits region, and  
140 numerical aspects of the model. To improve the representation of the inflow events, the bathymetry in the Danish Straits area  
141 was tuned. It is known that the narrow channels in the Straits (the Little Belt, Great Belt, and the Sound; Fig. 1c) play a crucial  
142 role in the water exchange between the North Sea and the Baltic Sea by allowing dense waters to creep to the Arkona basin.  
143 These channels are, however, very narrow and resolving them properly would require a much finer grid resolution (approx-  
144 imately 250 m; e.g., Stanev et al. 2018) than what is feasible in an operational model of the presented extent. Consequently, in  
145 coarser resolution configurations, the bathymetry must be tuned to facilitate the influx of dense water masses (e.g., She et al.,  
146 2007).

147 First, the bathymetry in the Great Belt was artificially deepened by a factor of 1.3 to allow the influx of dense waters. Next,  
148 the bathymetry was smoothed in the Danish Straits region between Kattegat and the Arkona basin by applying a Gaussian  
149 filter on the bathymetry raster field (using standard deviation  $\sigma$  of 2 grid cells). Large local gradients in the bathymetry field  
150 introduces local obstructions (“sills”) and also generates noise in the velocity field which tends to mix the tracers and thus  
151 reduce the pressure gradient driving the gravitational current. A less intrusive smoothing (a Gaussian filter with  $\sigma = 0.66$ ) was  
152 applied in the rest of the Baltic basin; our test runs indicate that a smoother bathymetry improves otherwise underestimated sea  
153 level variability in coastal regions, e.g. in the Gulf of Bothnia. Both the smoothing and deepening of the local bathymetry were  
154 necessary to reproduce Major Baltic Inflow events in the model.

155 In finite volume models, the accuracy of tracer and momentum advection schemes has a great impact on the effective  
156 numerical dissipation of the model. In the baroclinic regime, numerical models tend to generate noise at grid scale in the  
157 velocity field which tends to increase artificial mixing of tracers. Griffies and Hallberg (2000) and Ilıcak et al. (2012) have  
158 demonstrated that adding a suitable amount of viscosity can effectively suppress such oscillations in the velocity field, and  
159 therefore reduce the overall mixing of tracers. Moreover, higher order advection schemes can be utilized to reduce numerical  
160 mixing but they can also generate spurious, unphysical, oscillations in the advected quantity. In this work, we have chosen to  
161 use the 3rd order Upstream Biased Scheme (UBS), and the 4th order centered scheme, for horizontal and vertical advection





162 of momentum, respectively. The same advection scheme combination is used in ROMS (Regional Oceanic Modeling System;  
163 Shchepetkin and McWilliams 2005) as well. The UBS scheme adds some dissipation in the high-frequency part which reduces  
164 noise in the velocity field. The 4th order vertical scheme, on the other hand, is less dissipative and can retain sharp gradients  
165 better (e.g. in a stratified two-layer flow). For tracers, we use the 4th order Flux Corrected Transport (FCT) scheme in both  
166 horizontal and vertical directions; the vertical scheme uses the COMPACT formulation. The 4th order FCT schemes ensure  
167 lower numerical dissipation while being positive definite, i.e. they do not generate any spurious overshoots in the tracer fields.  
168 Switching to these higher-order advection schemes significantly improved the magnitude of salt inflow to the Arkona basin  
169 (not shown).

170 Our tests also indicated that the vertical eddy diffusivity from the turbulence model caused excessive vertical mixing in  
171 the Belt Sea–Arkona region, effectively stopping the propagation of the inflows. As a remedy, we lowered the Galperin limit  
172 parameter in the  $k - \varepsilon$  model to a value 0.10. In contrast, the value 0.17 was used in Nemo-Nordic 1.0 (Hordoir et al., 2019).

### 173 2.3 Forcings

174 The simulation covers a 2-year period from October 1, 2014 to September 30, 2016. Initial conditions for water temperature  
175 and salinity were obtained from a 14-month spin-up run (August 1, 2013 – September 30, 2014); SSH and velocity were  
176 initialized as zero. Because the model is initialized at rest, the first month of the simulation is excluded from the analysis and  
177 the model skill is evaluated for the remaining 23 months (November 1, 2014 to September 30, 2016).

178 The model is forced with the HIRLAM atmospheric forecast model data (<http://hirlam.org>, last access: March 29, 2021).  
179 The 10 m wind, 2 m air temperature, 2 m specific humidity, incoming long and short wave radiation, total precipitation, solid  
180 precipitation, and surface atmospheric pressure fields at 1 h temporal resolution are fed to the NEMO model. We use the NCAR  
181 bulk formulae (Large and Yeager, 2004) of the Aerobulk package (Brodeau et al., 2016) to evaluate the turbulent air–sea fluxes.  
182 In addition, atmospheric pressure gradient is applied in the momentum equation. To account for slightly underestimated wind  
183 speeds in the atmospheric model, the wind stress was multiplied by a factor 1.1 in NEMO.

184 Along the open boundaries in the North Sea, SSH, depth-averaged velocity, as well as vertical profiles of temperature and  
185 salinity are prescribed from the CMEMS Northwestern Shelf forecast model (Graham et al., 2018). This configuration is  
186 sufficient to prescribe the tidal signal in the North Sea, and sub-tidal variation of SSH, temperature and salinity.

187 River forcing data are obtained from the EHYPE model (Arheimer et al., 2012). River discharge and water temperature are  
188 prescribed at 729 rivers along the coasts with 1 day temporal resolution. Salinity of riverine water is set to zero.

### 189 2.4 Observations

190 Observational data was obtained from the Copernicus Marine Environment Monitoring Service (CMEMS) near-realtime, in-  
191 situ observation catalog (INSITU\_BAL\_NRT\_OBSERVATIONS\_013\_032). SSH data was obtained from 45 tide gauges  
192 across the whole Baltic basin (red markers in Fig. 1). Tide gauge SST observations were scarcer, focused more on the southern  
193 part of the basin (black markers). Vertical profile data of water temperature and salinity were obtained at locations shown  
194 with yellow markers. Only stations with more than 6 profiles in the study period were included in the analysis. In addition,



195 continuous vertical profile observations from the Arkona buoy (indicated by a yellow square in Fig. 1) were used; The data  
196 contain temperature and salinity observations at 1 h temporal resolution from eight CTDs at different depths (2 to 43 m).

197 FerryBox surface temperature and salinity observations were included from two ferries, TransPaper, and FinnMaid. As the  
198 observations have high sampling rate (typically  $< 30$  s), the data was binned to 10 min temporal resolution. The binned data  
199 consists of mean temperature, salinity, and ship location during the 10 min time window. Furthermore, the data was manually  
200 quality checked to remove spurious values (such as abnormally long periods showing constant salinity or temperature).

201 The salinity observations are in practical salinity units; for model skill analysis, observed salinity was converted to Absolute  
202 Salinity units. Prior to computing the error metrics, the model data was interpolated to the observation locations and time  
203 stamps. Unless otherwise specified, spatial interpolation was carried out with nearest neighbor search while linear interpolation  
204 was used in time.

205 Sea ice extent was computed from digitized ice charts by the Finnish Meteorological Institute. The ice chart frequency varied  
206 between 1 and 7 days in the study period. In the beginning of the ice season when ice coverage is scarce, ice charts are usually  
207 generated at 3 or 4 day intervals. Daily charts are typically available from late December onward.

## 208 2.5 Error metrics

209 The model skill is quantified with standard statistical measures. Let  $o_i$  and  $m_i$ ,  $i = 1, \dots, N$  be the observed and modeled time  
210 series, respectively. Denoting the mean of the time series by  $\bar{m}$ , the bias, Root Mean Square Deviation (RMSD) and Centered  
211 Root Mean Square Deviation (CRMSD) are defined as

$$212 \quad \text{BIAS} = \bar{m} - \bar{o},$$

$$213 \quad \text{RMSD}^2 = \frac{1}{N} \sum_{i=1}^N (m_i - o_i)^2,$$

$$214 \quad \text{CRMSD}^2 = \frac{1}{N} \sum_{i=1}^N ((m_i - \bar{m}) - (o_i - \bar{o}))^2.$$

215 Standard deviation ( $\sigma_m$ ) and correlation coefficient ( $R$ ) are given by

$$216 \quad \sigma_m^2 = \frac{1}{N} \sum_{i=1}^N (m_i - \bar{m})^2,$$

$$217 \quad R = \frac{1}{\sigma_o \sigma_m} \frac{1}{N} \sum_{i=1}^N (m_i - \bar{m})(o_i - \bar{o}).$$

218 CRMSD is related to  $\sigma_m$  and  $R$  though the equation,

$$219 \quad \text{CRMSD}^2 = \sigma_o^2 + \sigma_m^2 - \sigma_o \sigma_m R, \quad (2)$$





220 which can be visualized in a Taylor diagram (Taylor, 2001). In this work, we are normalizing the Taylor diagram by scaling  
221 the variables with  $\sigma_o$ :

$$222 \text{NCRMDS}^2 = 1 + \sigma_m'^2 - \sigma_m R, \quad (3)$$

$$223 \text{NCRMDS} = \frac{1}{\sigma_o} \text{CRMDS},$$

$$224 \sigma_m' = \frac{\sigma_m}{\sigma_o},$$

225 where NCRMDS and  $\sigma_m'$  are the normalized CRMDS and standard deviation of the model, respectively. Normalization leads  
226 into dimensionless metrics and permit comparison of different data sets in a single figure. As the Taylor diagram does  
227 not contain the bias, SST comparisons also include a target diagram depicting normalised bias,  $\text{NBIAS} = \text{BIAS}/\sigma_o$ , and  
228 NCRMDS. In the target diagram, NCRMDS has been augmented with the sign of  $\sigma_m - \sigma_o$ . We also use normalized RMSD,  
229  $\text{NRMSD} = \text{RMSD}/\sigma_o$ . NRMSD is a useful dimensionless metric: The value 1.0 can generally be regarded as a threshold for  
230 poor model skill. Indeed, setting  $m_i$  to the mean value of the observations results in  $\text{NRMSD}=1.0$ .

231 Comparing simulated SSH to observations is challenging. The exact vertical reference datum of the circulation model is not  
232 well defined. In addition, the available tide gauge data originates from different institutes that use different vertical datums.  
233 Although the observations can be converted to a common reference level, the modeled SSH is not directly comparable in terms  
234 of the mean elevation.

235 Simulated SSH depends on the forcing at the open boundaries, datum of model's bathymetry, riverine freshwater flux, and  
236 water density. At the open boundaries, we are using SSH from the Northwestern Shelf AMM model Graham et al. (2018). Its  
237 vertical reference is close to the mean sea level, but not exactly defined. Likewise, the GEBCO bathymetric data is nominally  
238 defined against local mean sea level, but in practice it consists of several local bathymetric datasets whose vertical datum may  
239 differ. Thus the modeled mean water depth and SSH may exhibit local biases, especially in coastal regions.

240 Because SSH bias is not a reliable model skill metric, SSH performance is therefore assessed with centralized metrics, e.g.  
241 CRMDS and Taylor diagrams.

## 242 3 Results

### 243 3.1 Sea surface height

244 SSH error metrics (CRMDS and standard deviation) are shown in Fig. 2. The model skill is generally good, CRMDS being  
245 below 10 cm at most stations. For the Baltic basin (Gulf of Bothnia, Gulf of Finland, Archipelago Sea, Gotland, Bornholm and  
246 Arkona basins), CRMDS is below 8 cm indicating that seiche waves are well reproduced. The only exception is Kronstadt,  
247 located at the eastern end of Gulf of Finland, where CRMDS is 10 cm. The deviation is generally larger in the Danish Straits  
248 and Kattegat/Skagerrak region where tidal variations are significant. The largest errors occur at Fredericia, in the Little Belt  
249 region, where CRMDS exceeds 12 cm. The model skill in these locations is affected by the Little Belt topography which is  
250 difficult to resolve at 1.8 km resolution; the strait itself is less than 1 km wide in the narrowest part. The model resolution

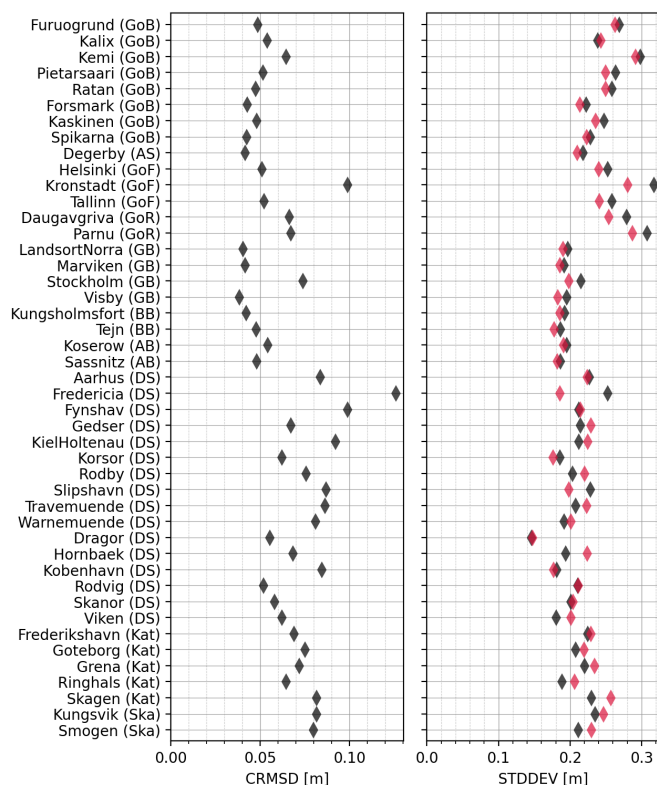


**Figure 2.** Sea surface height error metrics. Black and red symbols denote the model and observations, respectively. Sub-basins are indicated by the abbreviations: GoB, Gulf of Bothnia; AS, Archipelago Sea; GoF, Gulf of Finland; GB, Gotland Basin; BB, Bornholm Basin; AB, Arkona Basin; DS, Danish Straits; Kat, Kattegat; Ska, Skagerrak.

251 also affects the skill in other locations such as Kobenhavn in the Sound, and stations along the German coast of the Belt Sea  
252 (KielHoltenau, Warnemuende, Travemuende). All of these tide gauges are located inside an estuary mouth or harbor area which  
253 the present model cannot resolve.

254 In general, the model reproduces SSH standard deviation well (Fig. 2). The difference is within 2 cm in most cases; the  
255 largest deviation at Fredericia is approximately 7 cm. In the Baltic basin, the model has a tendency to overestimate variability.  
256 In the Danish Straits, the variability is slightly underestimated at several locations although overestimation also occurs.

257 The Taylor diagram (Fig. 3) shows that the model reproduces SSH variability well. Most stations have NCRMSD < 0.45,  
258 and the correlation coefficient is generally above 0.90. The deviations is the smallest in the Baltic basin where NCRMSD  
259 < 0.30 (except at Kronstadt and Stockholm) and the correlation coefficient is above 0.95 (except at Stockholm). The model  
260 performance at Stockholm is likely affected by the archipelago which is not fully resolved in the model. The Taylor diagram  
261 confirms that deviation is larger in the Danish Straits region; the worst stations are Fredericia in the Little Belt, as well as  
262 Kobenhavn.

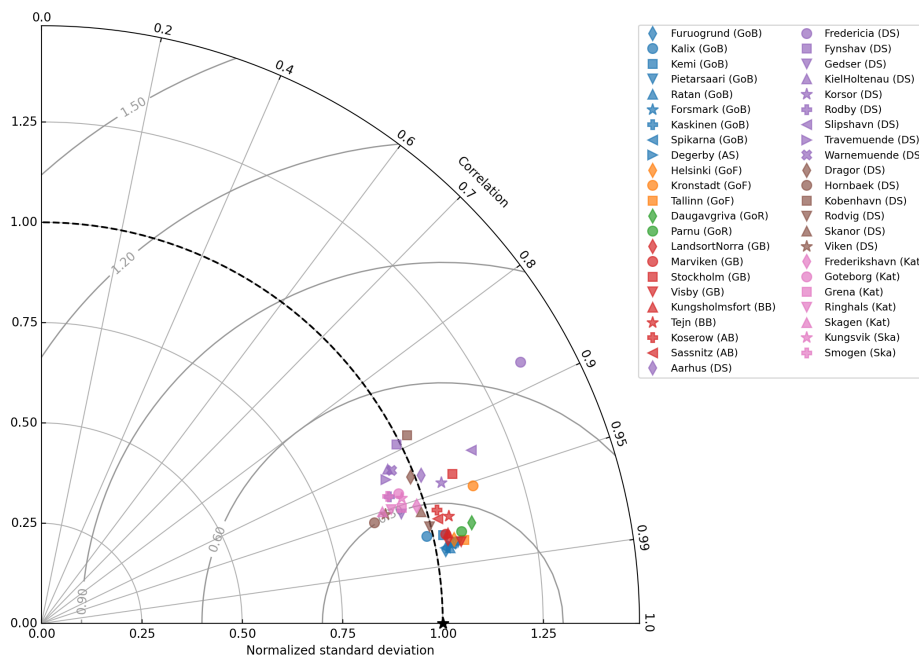


**Figure 3.** Taylor diagram of sea surface height error metrics. The metrics have been normalized by the standard deviation of the observations. The sub-basin abbreviations are as in Fig. 2.

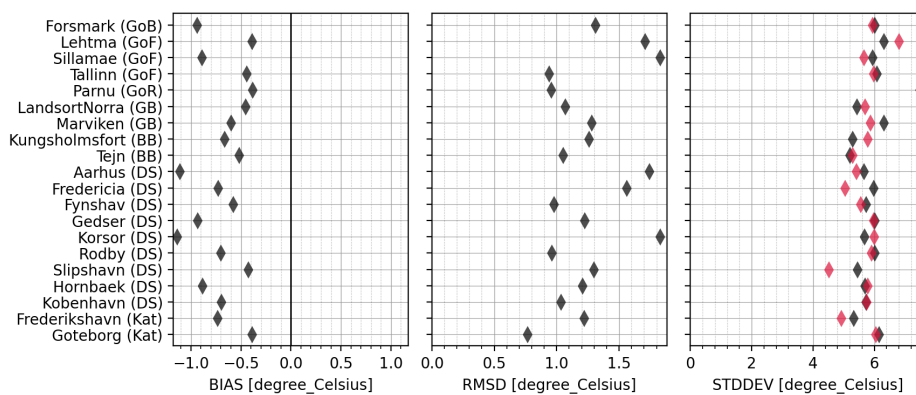


**Figure 4.** Surface temperature error metrics. Black and red symbols denote the model and observations, respectively. The sub-basin abbreviations are as in Fig. 2.

### 263 3.2 Sea Surface Temperature and Salinity

264 Sea surface temperature (SST) is mostly governed by surface heat fluxes, driven by the seasonal cycle of solar radiation and  
 265 air temperature, and vertical mixing. In addition, near the coast (where tide gauges are located), river discharge temperature

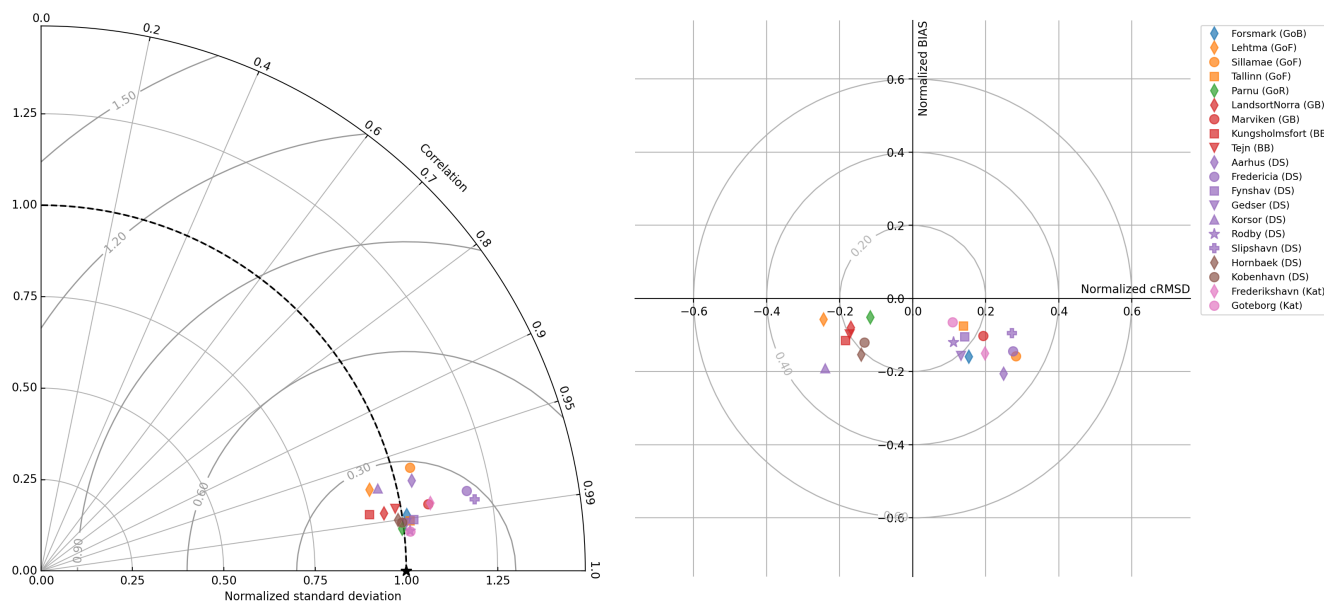


**Figure 5.** Taylor and target diagram of surface temperature error metrics. The metrics have been normalized by the standard deviation of the observations. The sub-basin abbreviations are as in Fig. 2.

266 can cause local variations. During summer, SST in shallow coastal regions can exceed 20°C. In the northern Baltic Sea, SST  
267 regularly reaches freezing point during winters.

268 Tide gauge SST metrics are shown in Fig. 4. In general, there is no clear pattern across the domain. The model has a  
269 negative bias (typically between -0.4 and -0.9°C) at almost all stations; the largest bias (exceeding -1.1°C) occurs at Korsor.  
270 The RMSD is below 1.9°C in all cases. The standard deviation is typically close to the observed value.

271 The Taylor diagram (Fig. 5, left) shows that SST skill is good in general. All locations are within 0.30 NCRMDS, and have  
272 a correlation coefficient above 0.95. The normalized standard deviation is generally close to unity except at Fredericia and  
273 Slipshavn. The model skill indicates that the model captures the seasonal SST variability well. The normalized target diagram  
274 (Fig. 5, right) shows that the negative bias is quite small (typically NBIAS < 0.20) compared to the overall SST variability (i.e.  
275 seasonal cycle).

276 Comparison against FerryBox SST from the TransPaper and FinnMaid ferries are shown in Figures 6 and 7, respectively (top  
277 row). Although the FerryBox data has sparser temporal coverage than the tide gauge observations, it is useful for validating  
278 the modeled SST in open waters away from the coasts. Also here the annual temperature cycle is well reproduced. The model  
279 bias is less than -0.5°C for the two ferries (Fig. 6c and 7c). RMSD is below 0.9°C, suggesting that SST performance is better  
280 in the open sea than at the tide gauge locations.

281 The TransPaper comparison shows a negative bias in the Baltic Proper and Gulf of Bothnia in summer 2015 (June–July; Fig.  
282 6 c). The bias is smaller during the following fall (October–December). A negative bias is visible in summer 2016 as well. The

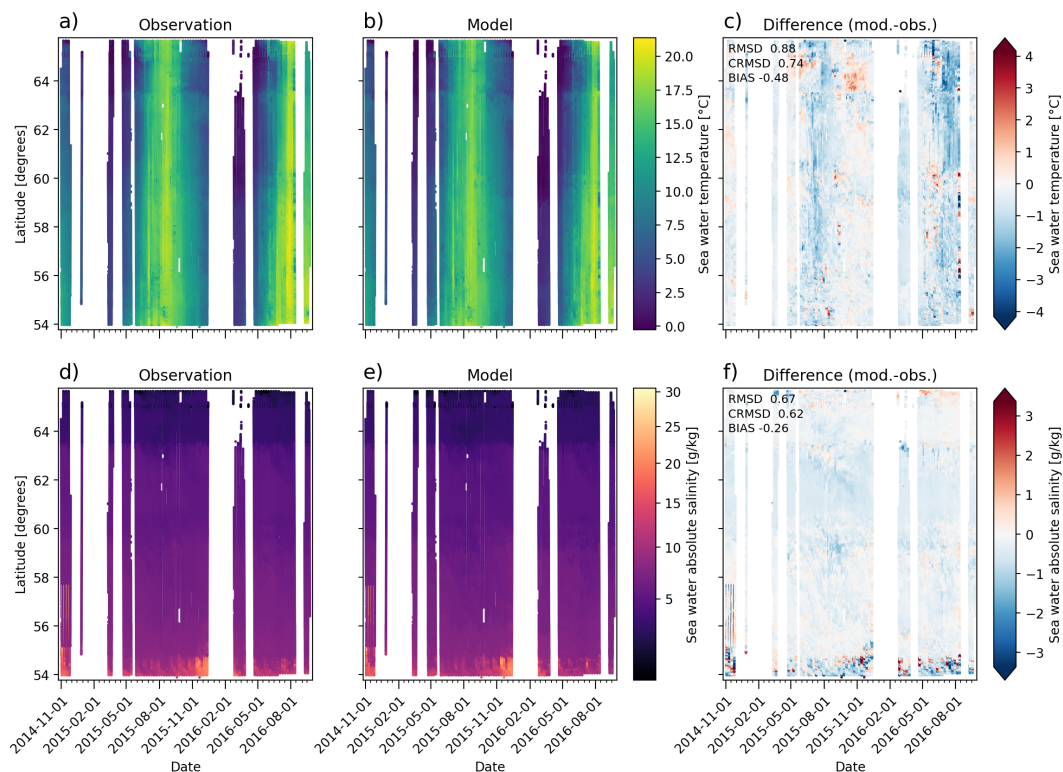


**Figure 6.** Surface temperature and salinity comparison against TransPaper FerryBox observations. The ferry operates between Oulu (top) and Lübeck (bottom). In the beginning of the data set (November 2014) the ferry also visited Gothenburg.

283 shorter FinnMaid data set also shows the negative bias during summer 2015 (Fig. 7 c). Although the data coverage is sparse,  
284 the comparison therefore suggest that the model has a negative bias during summer months (June–July) whereas the bias is  
285 smaller in fall. The magnitude of these deviations is, however, typically below 1.5°C.

286 FerryBox Sea surface salinity (SSS) comparison is shown in Figures 6 and 7 (bottom row). TransPaper observations (Fig.  
287 6d) clearly show the SSS gradient ranging from roughly 15 g/kg in the Belt Sea to 0 g/kg in the northern part of the Bothnian  
288 Bay. In November 2014, the ferry also visited Gothenburg where SSS can reach 30 g/kg. The model reproduces the salinity  
289 gradient well, bias is -0.26 g/kg and RMSD is 0.67 g/kg; In the FinnMaid data set (Fig. 7f), the bias and RMSD are similar,  
290 -0.16 and 0.55 g/kg, respectively. In both cases, the deviation is the largest in the Belt Sea and Kattegat where the model  
291 predominantly underestimates SSS. The larger error magnitude is due to the significant salinity gradients and their temporal  
292 variability in this region. The model has a small negative bias (-1 g/kg) in the Bothnian Sea (Fig. 6f). A negative bias is seen in  
293 the Gulf of Finland as well (around latitude 60°N; Fig. 7f).



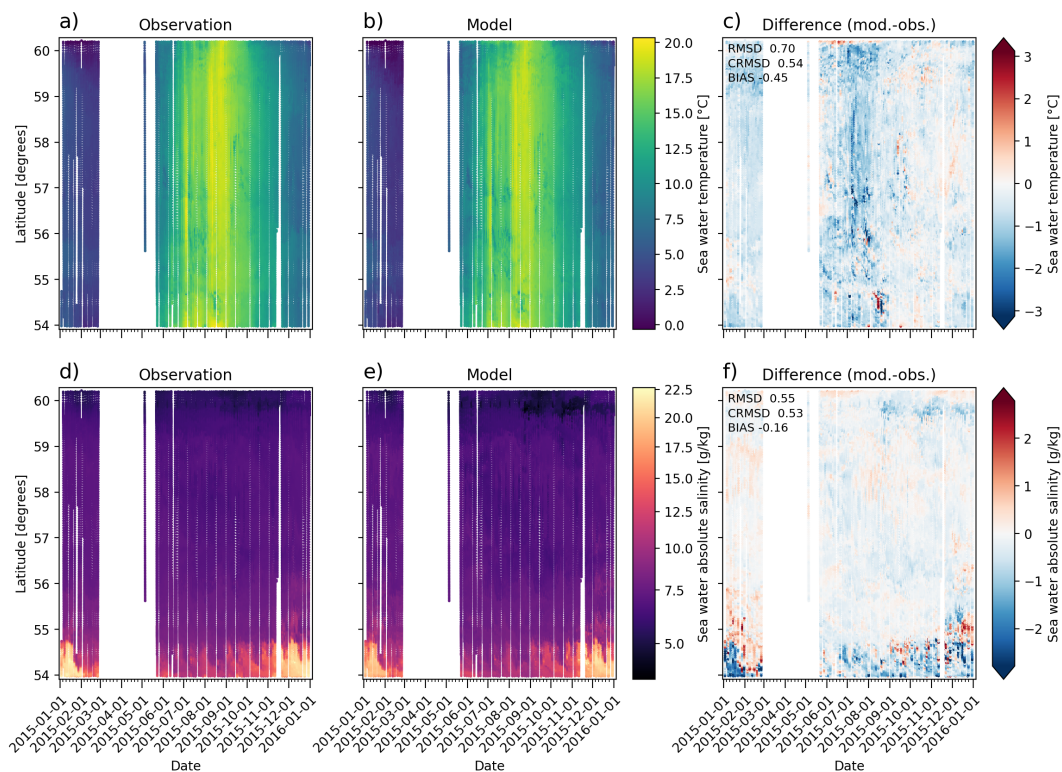


**Figure 7.** Surface temperature and salinity comparison against FinnMaid FerryBox observations. The ferry operates between Helsinki (top) and Lübeck (bottom).

### 294 3.3 Vertical profiles

295 Figure 8 shows comparison of temperature and salinity profiles against research vessel observations. In all panels, the outer  
296 ring denotes NRMSD, the middle ring RMSD, and the center dot the BIAS. RMSD and BIAS are visualized using the same  
297 color map; in all cases light color indicates small deviation. In addition, the metrics across all the plotted stations are printed in  
298 the upper left corner.

299 The temperature profile skill (Fig. 8a) is quite similar throughout the Baltic Sea. NRMSD is below 0.5 at all locations  
300 (except at C3 where NRMSD is 0.54) indicating good skill. The metrics for surface temperature (top 10 m; Fig. 8b) show low  
301 deviations. The NRMSD of the combined data set is 0.14 and bias is  $-0.51^{\circ}\text{C}$ . The high surface temperature skill is consistent  
302 with SST results presented in Sect. 3.2: the model can capture the seasonal surface temperature variability driven by the solar  
303 radiation. The profile comparison confirms that the skill is good in the entire surface layer.

304 The bottom temperature skill is poorer (Fig. 8c). RMSD in the Gotland basin is quite low (below  $0.5^{\circ}\text{C}$ ) while being higher  
305 in the Gulf of Finland and Gulf of Bothnia ( $0.6$  to  $1.3^{\circ}\text{C}$ ) In these regions, however, NRMSD exceeds value 2.0 at several  
306 stations: While RMSD is moderate, the deviation is significant compared to the low variability of bottom temperature. The bias



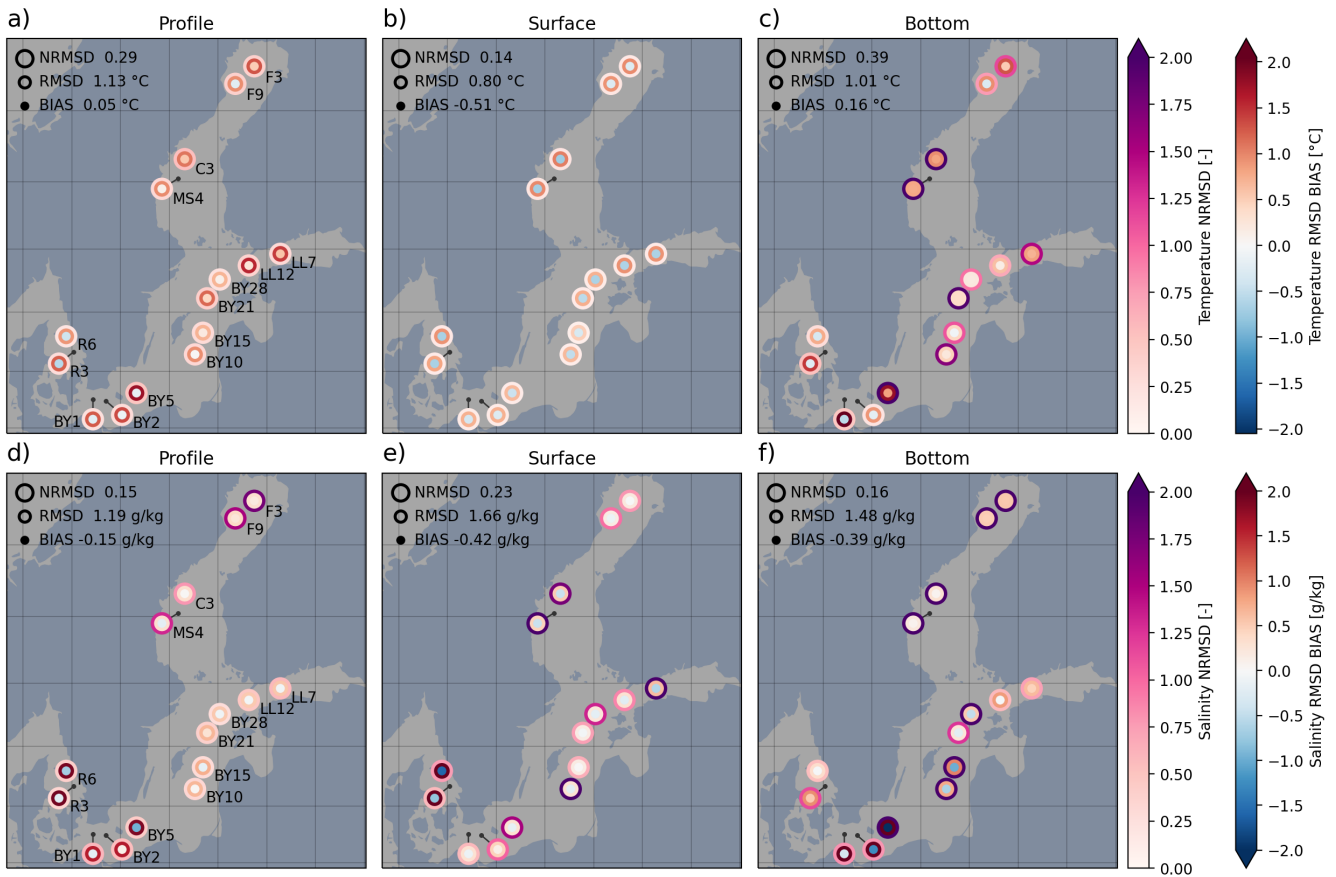


**Figure 8.** Vertical profile comparison against vessel observations; Temperature (top row) and salinity (bottom row). The dots depict NRMSD (outer ring), RMSD (inner ring), and BIAS (center dot). The metrics have been calculated for the entire profile (a,d), surface 10 m (b, e) and bottom (c, f). Combined metrics over all the stations is printed in each panel. Bottom values were computed for the lowest 15% of the water column.

307 tends to be positive in the Baltic basin, and negative in Kattegat and the Arkona basin. The largest deviation occurs at BY1  
 308 where RMSD reaches 2.0°C.

309 The model reproduces salinity profiles relatively well (Fig. 8d). The deviation is small (RMSD < 0.73 g/kg) in the Gotland  
 310 basin and Gulf of Finland. NRMSD is large in the Gulf of Bothnia due to the fact that salinity is low in this region as a result of  
 311 riverine freshwater input. In contrast, in the Danish Straits and Kattegat NRMSD is small while RMSD is relatively high (up  
 312 to 1.9 g/kg) due to the opposite reason: In this region, salinity regularly varies by more than 10 g/kg.

313 Surface salinity metrics (Fig. 8e) are generally similar to the whole profile metrics, except NRMSD is high in the Bothnian  
 314 Sea, Gulf of Finland, and southern Gotland basin.



315 The bottom salinity skill is presented in Fig. 8f. NRMSD regularly exceeds 2.0 in the Baltic basin because the variability of  
316 bottom salinity is small. A significant negative bias is visible in the Arkona and especially Bornholm basin; the bias is negative  
317 also in the Gotland basin. The deviation is moderate in Kattegat and the Gulf of Finland. While absolute deviation is small  
318 in the Gulf of Bothnia, NRMSD is large. In general, the results indicate that bottom salinity is underestimated in the Arkona,  
319 Bornholm, and Gotland basins. The skill is poorest in Bornholm (BY5). At this location, the model reproduces the halocline  
320 correctly but tends to underestimate bottom salinity. During the first simulated year the deviation is roughly  $-2$  g/kg; after  
321 November 2015 it is  $-4$  g/kg.

### 322 **3.4 The 2014 Major Baltic Inflow event**

323 A Major Baltic Inflow (MBI) event occurred in December, 2014. Mohrholz et al. (2015) divided the event into four phases:  
324 During the outflow period (November 7 – December 3 2014) strong easterly winds pushed surface waters from the Baltic  
325 Sea to Kattegat, lowering the mean sea level at Landsort by 57 cm. After the winds ceased for a couple of days, the inflow  
326 period was characterized by strong westerly winds. The precursory period (December 3 – December 13, 2014) brought saline  
327 waters through the Sound and into the Belt Sea. On December 13, the saline inflow had reached Darss Sill. At the buoy, the  
328 salinity exceeded 17 g/kg in the entire water column, marking the beginning of the main inflow period. The main inflow period  
329 lasted until December 25, 2014, when the westerly winds, and hence the barotropic inflow, ceased. During this time, the mean  
330 sea level at Landsort rose 95 cm from the lowest value, until the dense saline water mass had reached the Arkona basin. In  
331 the post-inflow period (starting on December 25, 2014), the saline water mass crept further into the Bornholm basin, and the  
332 following downstream sub-basins, driven by the baroclinic pressure gradient (density difference).

333 The observed salinity from the Arkona Buoy is shown in Figure 9 (panel a). The main salt pulse arrives at the buoy on  
334 December 16, 2014. On December 20, 2014, the dense water reaches 16 m depth. The model replicates the arrival of the  
335 pulse on December 16, 2014 and the main inflow phase (December 20 to December 26, 2014; Figure 9b). The bottom salinity  
336 is underestimated during the onset of the pulse (December 12 to 20 2014) from January 4 2015 onward (Figure 9c). Most  
337 notably, the observations show a secondary salt pulse in April 2015 which is underestimated in the model. The subsequent  
338 stronger pulses, in November 2015 and March 2016, are reproduced but their magnitude are also slightly underestimated. In  
339 general, the model captures the MBIs but has a tendency to underestimate salinity at the bottom, and overestimate it in the rest  
340 of the water column (up to 35 m depth).

341 A time series of bottom salinity at the Arkona Buoy is shown in Fig. 10 (panel a), accompanied by observations at BY5  
342 (Bornholm basin; panel b), BY10 (Gotland basin; panel c), and BY15 (Gotland deep; panel d). As stated above, the inflow  
343 reaches Arkona on December 16. First observation of elevated salinity at BY5 is from February 19 2015 but due to the gap in  
344 the measurements the pulse may have arrived earlier. At BY10 and BY15, an elevated bottom salinity is observed on February  
345 21 and March 17, respectively. The timing is quite well captured by the model: At Arkona the salt pulse is delayed by 1.5  
346 days. The modeled salt pulse reaches BY5 at the end of December 2014, BY10 in the end of February 2015 and BY15 in the  
347 beginning of March 2015. The model underestimates the maximum bottom salinity by roughly 2.5 g/kg at Arkona, 0.5 g/kg  
348 at BY5, 0.3 g/kg at BY10. The deviation, however, increases in time at BY5, BY10 and BY15. At BY5, the observed salinity

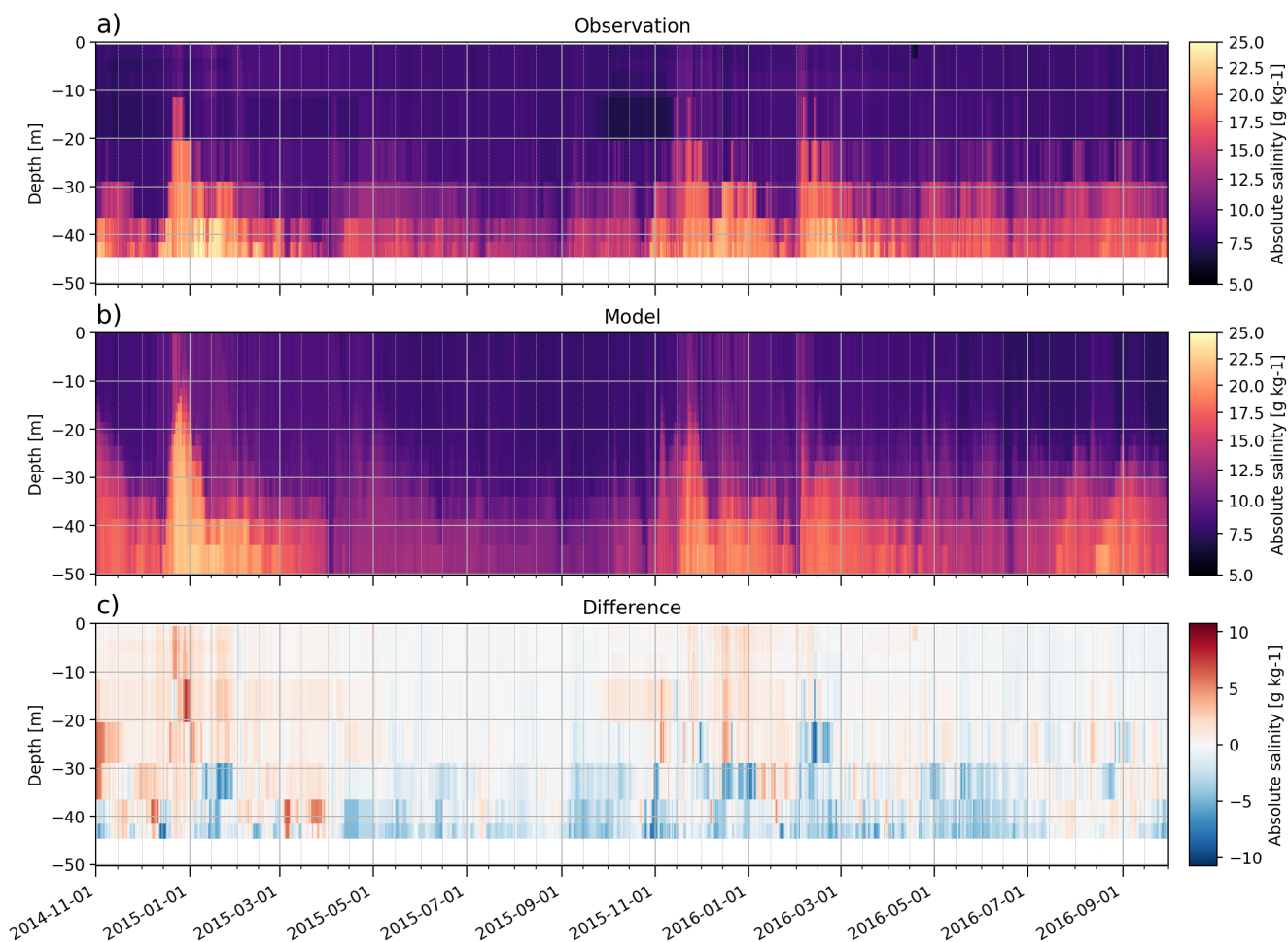


**Figure 9.** Vertical profile of salinity at Arkona. a) Observations; b) model; c) Difference (model - observations). The difference field has been computed by interpolating the model data to the observation locations.

349 remains above 18 g/kg (most of the time) after March 2015 while the modeled salinity decreases over time; in September 2016  
350 the model underestimates salinity by 4 g/kg.

351 A similar decrease in modeled salinity, although smaller in magnitude, is also seen at BY10 and BY15. The observations  
352 show a subsequent increase of bottom salinity (in February and April 2016 at BY15 and BY10, respectively) but the model  
353 does not capture these events. In summary, the results indicate that the model does reproduce magnitude and timings of the  
354 2014 MBI event and its propagation into the Baltic Proper. It does, however, underestimate the bottom salinity by 1 to 4 g/kg,  
355 and does not reproduce lesser MBI events observed in 2015 and 2016. The negative salinity bias is also seen in the profile  
356 statistics (Figure 8f).

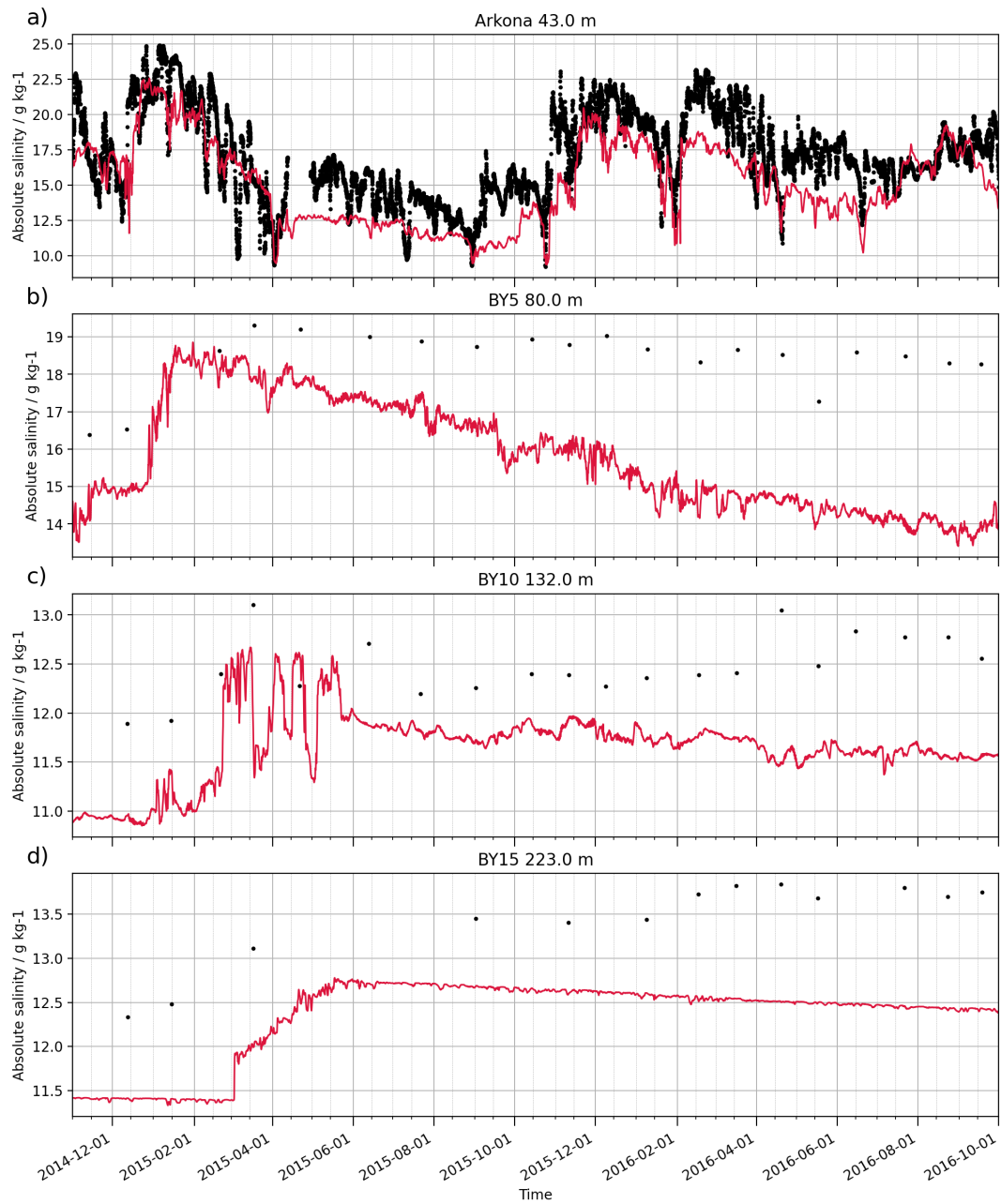


**Figure 10.** Time series of bottom salinity at selected locations. The red line denotes the model, the black dots are the observations.

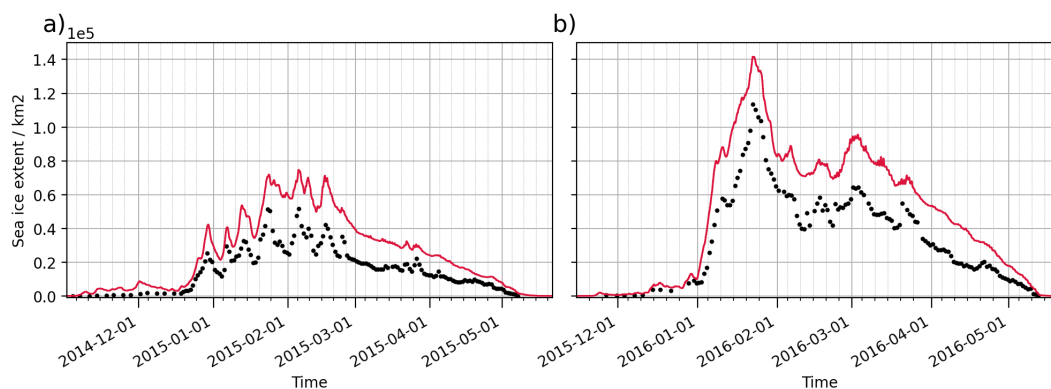


**Figure 11.** Time series of sea ice extent in the Baltic Sea for the two simulated winters. The red line denotes the model, the black dots are the observations.

### 357 3.5 Sea Ice

358 Sea ice extent (defined as the total area where sea ice concentration exceeds 15%) is presented in Fig. 11 for the winters  
359 2014/2015 (panel a) and 2015/2016 (b). The winter 2014/2015 was exceptionally mild with only about 50 000 km<sup>2</sup> sea ice  
360 extent whereas the winter 2015/2016 was quite typical; maximum ice extent, 120 000 km<sup>2</sup>, was observed in January 2016.  
361 During both winters, the model tended to overestimate the ice extent by roughly 25 000 km<sup>2</sup>. In relative numbers, the maximum  
362 ice extent was overestimated by 45% and 25% for the two winters, respectively. The ice season also started earlier in the model,  
363 especially in November 2014.

### 364 3.6 SSH under storm conditions

365 To assess how well the model is able to reproduce sea level variations under storm conditions, we analyze the Elon and Felix  
366 storms that occurred between January 7 and 12, 2015 (Fig. 12). The storms created strong westerly winds in the southern  
367 Baltic, with daily mean wind speed between 10 and 18 m s<sup>-1</sup>.

368 On January 8, westerly winds pushed water from the southern Baltic Sea to the east, lowering sea level in the Arkona basin  
369 and increasing it in the Gulf of Finland (event 1 in Fig. 12b,c); as the winds calmed, sea level at Helsinki retracted. The main  
370 storm event occurred on January 10, when strong westerly winds pushed water from the North Sea to Kattegat (Fig. 12d).  
371 Initially, sea levels rose in the Arkona basin (event 2A in Fig. 12c) but as winds prevailed and moved to the east, sea levels  
372 dropped by roughly 1.5 m in 12 h (2B). This led to a sea level increase in the Gulf of Finland and the Bothnian Sea (2B in Fig.  
373 12a,b). On January 11, northerly winds pushed water to the south, causing an opposite sea level change (event 3). This was  
374 followed by another weaker westerly wind event (event 4).

375 Overall the model captured the wind-driven water elevation variations in the southern Baltic Sea. The extremes are slightly  
376 underestimated: the maximum observed and simulated SSH range at Rodvig are 1.68 and 1.55 m, respectively. At Ringhals the

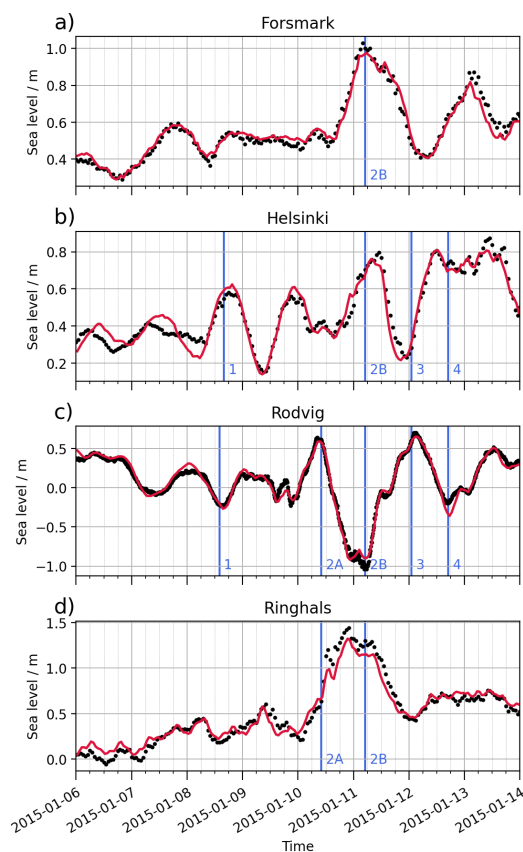


**Figure 12.** Time series of sea levels at selected locations during Elon and Felix storms. The red line denotes the model, the black dots are the observations. The model data has been bias corrected for visual comparison.

377 values are 1.40 and 1.27 m. The modeled seiche oscillations in Gulf of Bothnia and Gulf of Finland (Fig. 12a,b) are in good  
378 agreement with the observations. In Helsinki, the amplitude tends to be slightly overestimated and there's a phase lag of 1 to  
379 2 h. The tendency to underestimate SSH variability in the Danish Straits region, and overestimate it in the Baltic basin agrees  
380 well with the results of long-term validation using tide gauge data (Fig. 3).

381 To assess how well the model captures high and low SSH events during the entire simulation period, we identified five  
382 highest and five lowest SSH extremes in each tide gauge time series. The corresponding maximum/minimum SSH levels  
383 were identified from the model within a 6 h window from the observation extremum. Model's deviation from the observed  
384 peak/through was then calculated. Prior to the analysis, mean SSH was removed from both the observation and model data.  
385 The results are summarized in Fig. 13.

386 The model tends to underestimate high SSH values especially in the tidally dominated regions (Danish Straits, Kattegat, and  
387 Skagerrak). Low SSH values are similarly underestimated (i.e. positive deviation) in these regions. In general, the spread of the  
388 deviation is larger (up to 70 cm) in the tidally dominated regions while being small in the deeper basins (within 20 cm). The



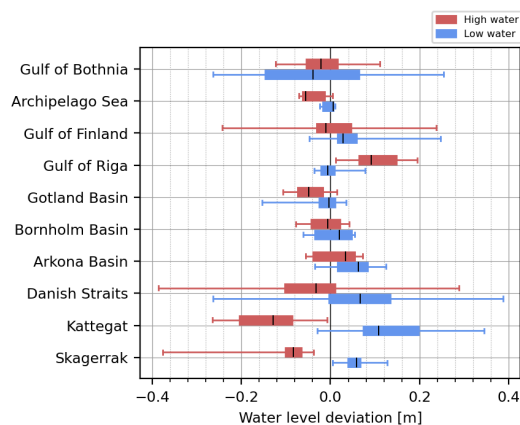


**Figure 13.** Model deviation in extreme water level cases in different sub-basins. Red and blue bars indicate model's deviation from the observed SSH maximum and minimum, respectively. Positive values mean that the modeled SSH is higher. The thin line denotes the entire deviation range; thick bars indicate the 25 to 75 percentile range. Black line denotes the mean. The sub-basins are defined as in Fig. 2.

389 spread is larger in the Gulf of Bothnia and Gulf of Finland due to SSH build up in these elongated basins. High SSH events are  
390 overestimated in the Gulf of Riga. These results confirm that the model tends to underestimate SSH variability in the Danish  
391 waters while it is slightly overestimated in the Gulf of Bothnia and Gulf of Finland.

#### 392 4 Discussion and conclusions

393 The presented model validation for the 23 month period (November 1, 2014 – September 30, 2016) shows that the model  
394 reproduces SSH variability well. Model skill in the Baltic basin is especially good: CRMSD is typically below 7 cm. In the  
395 Danish Straits region, the deviation is larger due to the interaction of the tides and the complex topography. It is worth noting  
396 that many tide gauges are located in harbor or river mouth regions, or in small coastal embayments which cannot be properly  
397 resolved at the used resolution. The model has a tendency to underestimate SSH extremes especially under storm conditions.  
398 This is attributable to the atmospheric forcing data which generally tends to underestimate extremes during storm events, as  
399 well as to the model's dissipation (e.g., caused by coarse grid resolution, or friction parameterization).

400 The SST and SSS skill is generally good. The FerryBox comparison resulted in RMSD of 0.9°C and 0.70 g/kg, respectively.  
401 SST, however, shows a systematic negative bias of approximately -0.5°C. Our calibration runs suggest that the negative SST  
402 bias can be related to underestimated vertical mixing. Another possible cause is river runoff temperature which has a strong  
403 impact on SST in the vicinity of the river mouth. Yet another possibility is the downward longwave radiation forcing from the  
404 atmospheric model. The temperature deviation is larger in the bottom where RMSD can exceed 2°C.

405 The model tends to overestimate sea ice extent by 25 to 45%. As ice growth is strongly affected by SST, the overestimation  
406 is likely affected by the negative SST bias. Our calibration runs indicate that the sea ice model parameters have only a minor  
407 effect on the sea ice extent. Further research is needed to improve the biases in SST and sea ice.



408 The model replicates the 2014 MBI event and subsequent inflows in 2015 and 2016. The timing and magnitude of the MBI  
409 salt pulse at Arkona compares well with observations and the bottom salinity is only slightly underestimated. In the Bornholm  
410 Basin, the MBI is relatively well simulated by the model, especially considering that the initial bottom salinity is slightly low.  
411 After the inflow, however, the modelled bottom salinity decreases at a semi-constant rate, and much faster than in reality. There  
412 could be several reasons for this. First, it is possible that the vertical resolution is too coarse in the deeper layers (see discussion  
413 below), leading to too high vertical numerical diffusion. Second, the fast decline in bottom salinity could be due to an absence  
414 of smaller inflows after the MBI, which the model is not able to simulate well enough. Third, the type of vertical discretization  
415 employed in the model ( $z^*$  coordinates) is not so well suited to simulate dense bottom currents over rough topography, which  
416 may lead to a spurious vertical circulation (Dietze et al., 2014). Smoothing of the topography between the Arkona Basin and  
417 the Bornholm Basin may help in this respect.

418 The volume and propagation of the inflow can also be affected by the horizontal resolution: Inflow through the Sound, for  
419 example, is significant, contributing 20 to 30% of the total volume (Mohrholz et al., 2015), yet it is difficult to resolve the  
420 narrow strait in operational models (Fischer and Matthäus, 1996; She et al., 2007; Gräwe et al., 2015b).

421 While both the Nemo-Nordic 1.0 and 2.0 versions use 56 vertical levels, their thickness distributions are different. In the 2.0  
422 configuration, the surface resolution has been increased from 3 to 1 m in the top 10 m, implying coarser resolution between 50  
423 and 200 m depths. Our calibration runs with 75 and 100 vertical levels indicate that higher vertical resolution in 40 to 100 m  
424 range improves bottom salinity in the Bornholm basin (not shown). In addition, the strength of the salt inflow is sensitive to the  
425 bathymetry in the Danish Straits region (smoothing the bathymetry and deepening the channels), the used advection schemes  
426 (UBS for momentum advection), as well as turbulence closure parameters (lowering the Galperin limit). Thus, horizontal and  
427 vertical grid resolution, numerical mixing and turbulence parameterizations all play important roles in simulating the inflow  
428 dynamics. MBI dynamics will be studied in more detail in the future.

429 From operational modeling perspective, the presented model configuration provides adequate skill for forecasting. SSH skill  
430 is good in the entire Baltic basin and generally comparable to other models. It is worth noting that in short-term forecasts the  
431 SSH skill is also highly dependent on the quality of the atmospheric forcing. SST and salinity biases are small or moderate and  
432 those can be corrected with data-assimilation. Surface currents are an important product of operational forecasts, used in several  
433 applications, such as oil drift modeling. Validating modeled currents, however, is challenging due to the lack of measurements  
434 with sufficient spatial and temporal coverage. Comparing simulated currents at 1 nautical mile grid resolution against point  
435 measurements poses additional challenges (Lagemaa et al., 2010). Nevertheless, the model's ability to simulate SSH, water  
436 temperature and salinity demonstrates that the general circulation and dynamics are captured fairly well even though direct  
437 validation of surface currents was not possible.

438 Improving the model skill is an ongoing effort. The bathymetry can be further improved to better represent the coast line  
439 and shallow coastal regions, as well as unresolved channels. The wetting and drying capability of NEMO (O'Dea et al., 2020)  
440 could improve SSH in shallow regions. Using higher vertical resolution will likely result in improved salt inflow dynamics.  
441 Further work is needed to calibrate advection schemes, diffusion parameterizations, and the representations of overflows to  
442 reduce numerical mixing. Most notably, adopting high resolution nesting in strategic regions, such as the Danish Straits and



443 the Archipelago Sea could greatly improve the representation of water exchange processes. Finally, data assimilation and online  
444 coupling with atmospheric models can be used to improve both the forecast and reanalysis products.

445 *Code availability.* Nemo-Nordic is based on the NEMO source code version 4.0 (subversion trunk revision 11281), released under the open  
446 source CeCill license (<https://cecill.info>, last access: March 29, 2021). The standard NEMO source code can be downloaded from the NEMO  
447 website (<http://www.nemo-ocean.eu/>, last access: March 29, 2021). The Nemo-Nordic source code used in the present article has been  
448 archived on Zenodo (Nemo-Nordic development team, 2021).

449 *Author contributions.* All authors contributed to the conceptualization of the model configuration, parameter tuning and validation. SF, PaL,  
450 TK, LA, and IR implemented changes in the model source code, implemented the model configuration and processed forcing data. TK, PaL,  
451 SF, LA, IR, IM, AL, SJS, SV contributed to model validation and tuning. TK was responsible for the original draft of the manuscript and  
452 data visualization. TK, LA, IR, LT, VH, SF contributed to the review and editing of the manuscript. AN, VH, LT, PrL, and IL contributed to  
453 the administration and supervision of the operational model development activities within the CMEMS BAL MFC project.

454 *Competing interests.* The authors declare that they have no conflict of interest.

455 *Acknowledgements.* This work is supported by the Copernicus Marine Environment Monitoring Service (CMEMS). Observational data was  
456 provided by DMI, BSH, SHMI, MSI, LEGMA and FMI. This data was collected and made freely available by the Copernicus project and  
457 programmes that contribute to it. Data analysis and visualization were carried out with Matplotlib (Hunter, 2007) and Iris (Met Office, 2010  
458 - 2020) Python packages. The authors wish to acknowledge CSC – IT Center for Science, Finland, for computational resources.



## 459 References

- 460 Arheimer, B., Dahné, J., Donnelly, C., Lindström, G., and Strömqvist, J.: Water and nutrient simulations using the HYPE model for Sweden  
461 vs. the Baltic Sea basin – influence of input-data quality and scale, *Hydrology Research*, 43, 315–329, <https://doi.org/10.2166/nh.2012.010>,  
462 <https://doi.org/10.2166/nh.2012.010>, 2012.
- 463 Axell, L.: BSRA-15: A Baltic Sea Reanalysis 1990–2004, Reports Oceanography 45, Swedish Meteorological and Hydrological Institute,  
464 SE–601 76 Norrköping, Sweden, 2013.
- 465 Berg, P. and Poulsen, J. W.: Implementation details for HBM, Tech. rep., Danish Meteorological Institute, 2012.
- 466 Brodeau, L., Barnier, B., Gulev, S. K., and Woods, C.: Climatologically Significant Effects of Some Approximations in the Bulk Pa-  
467 rameterizations of Turbulent Air–Sea Fluxes, *Journal of Physical Oceanography*, 47, 5–28, <https://doi.org/10.1175/jpo-d-16-0169.1>,  
468 <https://doi.org/10.1175/jpo-d-16-0169.1>, 2016.
- 469 Daewel, U. and Schrum, C.: Simulating long-term dynamics of the coupled North Sea and Baltic Sea ecosystem with ECOSMO II: Model  
470 description and validation, *Journal of Marine Systems*, 119–120, 30–49, <https://doi.org/10.1016/j.jmarsys.2013.03.008>, <https://doi.org/10.1016/j.jmarsys.2013.03.008>, 2013.
- 472 Dietze, H., Löptien, U., and Getzlaff, K.: MOMBA 1.1 – a high-resolution Baltic Sea configuration of GFDL's Modular Ocean Model,  
473 *Geoscientific Model Development*, 7, 1713–1731, <https://doi.org/10.5194/gmd-7-1713-2014>, <https://doi.org/10.5194/gmd-7-1713-2014>,  
474 2014.
- 475 Fischer, H. and Matthäus, W.: The importance of the Drogden Sill in the Sound for major Baltic inflows, *Journal of Marine Systems*, 9,  
476 137–157, [https://doi.org/10.1016/s0924-7963\(96\)00046-2](https://doi.org/10.1016/s0924-7963(96)00046-2), [https://doi.org/10.1016/s0924-7963\(96\)00046-2](https://doi.org/10.1016/s0924-7963(96)00046-2), 1996.
- 477 Funkquist, L. and Kleine, E.: HIROMB: An introduction to HIROMB, an operational baroclinic model for the Baltic Sea, Reports Oceanog-  
478 raphy 37, Swedish Meteorological and Hydrological Institute, SE–601 76 Norrköping, Sweden, 2007.
- 479 Graham, J. A., O’Dea, E., Holt, J., Polton, J., Hewitt, H. T., Furner, R., Guihou, K., Brereton, A., Arnold, A., Wakelin, S., Sanchez, J. M. C.,  
480 and Adame, C. G. M.: AMM15: a new high-resolution NEMO configuration for operational simulation of the European north-west shelf,  
481 *Geoscientific Model Development*, 11, 681–696, <https://doi.org/10.5194/gmd-11-681-2018>, <https://doi.org/10.5194/gmd-11-681-2018>,  
482 2018.
- 483 Gräwe, U., Holtermann, P., Klingbeil, K., and Burchard, H.: Advantages of vertically adaptive coordinates in numerical models of stratified  
484 shelf seas, *Ocean Modelling*, 92, 56–68, <https://doi.org/10.1016/j.ocemod.2015.05.008>, <https://doi.org/10.1016/j.ocemod.2015.05.008>,  
485 2015a.
- 486 Gräwe, U., Naumann, M., Mohrholz, V., and Burchard, H.: Anatomizing one of the largest saltwater inflows into the Baltic Sea in De-  
487 cember 2014, *Journal of Geophysical Research: Oceans*, 120, 7676–7697, <https://doi.org/10.1002/2015jc011269>, [https://doi.org/10.1002/](https://doi.org/10.1002/2015jc011269)  
488 [2015jc011269](https://doi.org/10.1002/2015jc011269), 2015b.
- 489 Griffies, S. M. and Hallberg, R. W.: Biharmonic Friction with a Smagorinsky-Like Viscosity for Use in Large-Scale Eddy-Permitting Ocean  
490 Models, *Monthly Weather Review*, 128, 2935–2946, [https://doi.org/10.1175/1520-0493\(2000\)128<2935:bfwasl>2.0.co;2](https://doi.org/10.1175/1520-0493(2000)128<2935:bfwasl>2.0.co;2), [https://doi.org/](https://doi.org/10.1175/1520-0493(2000)128<2935:bfwasl>2.0.co;2)  
491 [10.1175/1520-0493\(2000\)128<2935:bfwasl>2.0.co;2](https://doi.org/10.1175/1520-0493(2000)128<2935:bfwasl>2.0.co;2), 2000.
- 492 Gustafsson, B.: Interaction between Baltic Sea and North Sea, *Deutsche Hydrographische Zeitschrift*, 49, 165–183,  
493 <https://doi.org/10.1007/bf02764031>, <https://doi.org/10.1007/bf02764031>, 1997.



- 494 Gustafsson, B. G. and Andersson, H. C.: Modeling the exchange of the Baltic Sea from the meridional atmospheric pressure difference across  
495 the North Sea, *Journal of Geophysical Research: Oceans*, 106, 19 731–19 744, <https://doi.org/10.1029/2000jc000593>, <https://doi.org/10.1029/2000jc000593>, 2001.
- 497 Hofmeister, R., Beckers, J.-M., and Burchard, H.: Realistic modelling of the exceptional inflows into the central Baltic Sea in 2003 using  
498 terrain-following coordinates, *Ocean Modelling*, 39, 233–247, <https://doi.org/10.1016/j.ocemod.2011.04.007>, [https://doi.org/10.1016/j.](https://doi.org/10.1016/j.ocemod.2011.04.007)  
499 [ocemod.2011.04.007](https://doi.org/10.1016/j.ocemod.2011.04.007), 2011.
- 500 Hordoir, R., Axell, L., Höglund, A., Dieterich, C., Fransner, F., Gröger, M., Liu, Y., Pemberton, P., Schimanke, S., Andersson, H., Ljunge-  
501 myr, P., Nygren, P., Falahat, S., Nord, A., Jönsson, A., Lake, I., Döös, K., Hieronymus, M., Dietze, H., Löptien, U., Kuznetsov, I.,  
502 Westerlund, A., Tuomi, L., and Haapala, J.: Nemo-Nordic 1.0: a NEMO-based ocean model for the Baltic and North seas – re-  
503 search and operational applications, *Geoscientific Model Development*, 12, 363–386, <https://doi.org/10.5194/gmd-12-363-2019>, <https://doi.org/10.5194/gmd-12-363-2019>, 2019.
- 505 Hourdin, F. and Armengaud, A.: The Use of Finite-Volume Methods for Atmospheric Advection of Trace Species. Part I: Test  
506 of Various Formulations in a General Circulation Model, *Monthly Weather Review*, 127, 822–837, [https://doi.org/10.1175/1520-0493\(1999\)127<0822:tuofvm>2.0.co;2](https://doi.org/10.1175/1520-0493(1999)127<0822:tuofvm>2.0.co;2), [https://doi.org/10.1175/1520-0493\(1999\)127<0822:tuofvm>2.0.co;2](https://doi.org/10.1175/1520-0493(1999)127<0822:tuofvm>2.0.co;2), 1999.
- 508 Hunter, J. D.: Matplotlib: A 2D graphics environment, *Computing in Science & Engineering*, 9, 90–95,  
509 <https://doi.org/10.1109/MCSE.2007.55>, 2007.
- 510 Huthnance, J.: Physical oceanography of the North Sea, *Ocean and Shoreline Management*, 16, 199–231, [https://doi.org/10.1016/0951-8312\(91\)90005-m](https://doi.org/10.1016/0951-8312(91)90005-m), [https://doi.org/10.1016/0951-8312\(91\)90005-m](https://doi.org/10.1016/0951-8312(91)90005-m), 1991.
- 512 Ilıcak, M., Adcroft, A. J., Griffies, S. M., and Hallberg, R. W.: Spurious diapycnal mixing and the role of momentum closure, *Ocean*  
513 *Modelling*, 45–46, 37–58, <https://doi.org/10.1016/j.ocemod.2011.10.003>, <https://doi.org/10.1016/j.ocemod.2011.10.003>, 2012.
- 514 IOC, SCOR, I.: The International thermodynamic equation of seawater–2010: calculation and use of thermodynamic properties. [includes  
515 corrections up to 31st October 2015], Intergovernmental Oceanographic Commission, Manuals and Guides Nb. 56, 2010.
- 516 Lagemaat, P., Suhhova, I., Nomm, M., Pavelson, J., and Elken, J.: Comparison of current simulations by the state-of-the-art operational  
517 models in the Gulf of Finland with ADCP measurements, in: 2010 IEEE/OES Baltic International Symposium (BALTIC), IEEE,  
518 <https://doi.org/10.1109/baltic.2010.5621656>, <https://doi.org/10.1109/baltic.2010.5621656>, 2010.
- 519 Large, W. and Yeager, S.: Diurnal to decadal global forcing for ocean and sea-ice models: The data sets and flux climatologies, Tech. rep.,  
520 National Center for Atmospheric Research, Boulder, Colorado, United States, <https://doi.org/10.5065/D6KK98Q6>, <http://opensky.ucar.edu/islandora/object/technotes:434>, 2004.
- 522 Lehmann, A.: A three-dimensional baroclinic eddy-resolving model of the Baltic Sea, *Tellus A: Dynamic Meteorology and Oceanography*,  
523 47, 1013–1031, <https://doi.org/10.3402/tellusa.v47i5.11969>, <https://doi.org/10.3402/tellusa.v47i5.11969>, 1995.
- 524 Lemieux, J.-F., Dupont, F., Blain, P., Roy, F., Smith, G. C., and Flato, G. M.: Improving the simulation of landfast ice by com-  
525 bining tensile strength and a parameterization for grounded ridges, *Journal of Geophysical Research: Oceans*, 121, 7354–7368,  
526 <https://doi.org/10.1002/2016jc012006>, <https://doi.org/10.1002/2016jc012006>, 2016.
- 527 Leppäranta, M. and Myrberg, K.: Physical oceanography of the Baltic Sea, Springer Science & Business Media,  
528 <https://doi.org/https://doi.org/10.1007/978-3-540-79703-6>, 2009.
- 529 Lévy, M., Estublier, A., and Madec, G.: Choice of an advection scheme for biogeochemical models, *Geophysical Research Letters*, 28,  
530 3725–3728, <https://doi.org/10.1029/2001gl012947>, <https://doi.org/10.1029/2001gl012947>, 2001.



- 531 Madec, G., Bourdallé-Badie, R., Chanut, J., Clementi, E., Coward, A., Ethé, C., Iovino, D., Lea, D., Lévy, C., Lovato, T., Martin, N., Masson,  
532 S., Mocavero, S., Rousset, C., Storkey, D., Vancoppenolle, M., Müeller, S., Nurser, G., Bell, M., and Samson, G.: NEMO ocean engine,  
533 <https://doi.org/10.5281/zenodo.3878122>, <https://doi.org/10.5281/zenodo.3878122>, 2019.
- 534 Meier, M., Doescher, R., Coward, A. C., Nycander, J., and Döös, K.: RCO – Rossby Centre regional Ocean climate model: model description  
535 (version 1.0) and first results from the hindcast period 1992/93, Tech. Rep. 26, SMHI, 1999.
- 536 Met Office: Iris: A Python package for analysing and visualising meteorological and oceanographic data sets, Exeter, Devon, v2.4 edn.,  
537 <https://scitools.org.uk/iris/docs/v2.4.0/>, 2010 - 2020.
- 538 Mohrholz, V.: Major Baltic Inflow Statistics – Revised, *Frontiers in Marine Science*, 5, <https://doi.org/10.3389/fmars.2018.00384>, <https://doi.org/10.3389/fmars.2018.00384>, 2018.
- 540 Mohrholz, V., Naumann, M., Nausch, G., Krüger, S., and Gräwe, U.: Fresh oxygen for the Baltic Sea — An exceptional saline inflow after a  
541 decade of stagnation, *Journal of Marine Systems*, 148, 152–166, <https://doi.org/10.1016/j.jmarsys.2015.03.005>, <https://doi.org/10.1016/j.jmarsys.2015.03.005>, 2015.
- 543 Nemo-Nordic development team: Nemo-Nordic ocean model source code (Version 2.0), <https://doi.org/10.5281/zenodo.4665840>, <https://doi.org/10.5281/zenodo.4665840>, 2021.
- 545 O’Dea, E., Bell, M. J., Coward, A., and Holt, J.: Implementation and assessment of a flux limiter based wetting and drying scheme in NEMO,  
546 *Ocean Modelling*, 155, 101–108, <https://doi.org/10.1016/j.ocemod.2020.101708>, <https://doi.org/10.1016/j.ocemod.2020.101708>, 2020.
- 547 Pätsch, J., Burchard, H., Dieterich, C., Gräwe, U., Gröger, M., Mathis, M., Kapitza, H., Bersch, M., Moll, A., Pohlmann, T., Su, J., Ho-  
548 Hagemann, H. T., Schulz, A., Elizalde, A., and Eden, C.: An evaluation of the North Sea circulation in global and regional models  
549 relevant for ecosystem simulations, *Ocean Modelling*, 116, 70–95, <https://doi.org/10.1016/j.ocemod.2017.06.005>, <https://doi.org/10.1016/j.ocemod.2017.06.005>, 2017.
- 551 Pemberton, P., Löptien, U., Hordoir, R., Höglund, A., Schimanke, S., Axell, L., and Haapala, J.: Sea-ice evaluation of NEMO-Nordic 1.0: a  
552 NEMO-LIM3.6-based ocean–sea-ice model setup for the North Sea and Baltic Sea, *Geoscientific Model Development*, 10, 3105–3123,  
553 <https://doi.org/10.5194/gmd-10-3105-2017>, <https://doi.org/10.5194/gmd-10-3105-2017>, 2017.
- 554 Reffray, G., Bourdalle-Badie, R., and Calone, C.: Modelling turbulent vertical mixing sensitivity using a 1-D version of NEMO, *Geoscientific*  
555 *Model Development*, 8, 69–86, <https://doi.org/10.5194/gmd-8-69-2015>, <https://doi.org/10.5194/gmd-8-69-2015>, 2015.
- 556 Roquet, F., Madec, G., McDougall, T. J., and Barker, P. M.: Accurate polynomial expressions for the density and specific volume of sea-  
557 water using the TEOS-10 standard, *Ocean Modelling*, 90, 29–43, <https://doi.org/10.1016/j.ocemod.2015.04.002>, <https://doi.org/10.1016/j.ocemod.2015.04.002>, 2015.
- 559 Shchepetkin, A. F. and McWilliams, J. C.: The regional oceanic modeling system (ROMS): a split-explicit, free-surface, topography-  
560 following-coordinate oceanic model, *Ocean Modelling*, 9, 347–404, <https://doi.org/10.1016/j.ocemod.2004.08.002>, <https://doi.org/10.1016/j.ocemod.2004.08.002>, 2005.
- 562 She, J., Berg, P., and Berg, J.: Bathymetry impacts on water exchange modelling through the Danish Straits, *Journal of Marine Systems*, 65,  
563 450–459, <https://doi.org/10.1016/j.jmarsys.2006.01.017>, <https://doi.org/10.1016/j.jmarsys.2006.01.017>, 2007.
- 564 She, J., Meier, H. E. M., Darecki, M., Gorringe, P., Huess, V., Kouts, T., Reissmann, J. H., and Tuomi, L.: Baltic Sea Operational  
565 Oceanography—A Stimulant for Regional Earth System Research, *Frontiers in Earth Science*, 8, <https://doi.org/10.3389/feart.2020.00007>,  
566 <https://doi.org/10.3389/feart.2020.00007>, 2020.
- 567 Stanev, E., Pein, J., Grashorn, S., Zhang, Y., and Schrum, C.: Dynamics of the Baltic Sea straits via numerical simulation of exchange flows,  
568 *Ocean Modelling*, 131, 40–58, <https://doi.org/10.1016/j.ocemod.2018.08.009>, <https://doi.org/10.1016/j.ocemod.2018.08.009>, 2018.





- 569 Taylor, K. E.: Summarizing multiple aspects of model performance in a single diagram, *Journal of Geophysical Research: Atmospheres*, 106,  
570 7183–7192, <https://doi.org/10.1029/2000jd900719>, <https://doi.org/10.1029/2000jd900719>, 2001.
- 571 Umlauf, L. and Burchard, H.: A generic length-scale equation for geophysical turbulence models, *Journal of Marine Research*, 61, 235–265,  
572 <https://doi.org/10.1357/002224003322005087>, <https://doi.org/10.1357/002224003322005087>, 2003.
- 573 Vancoppenolle, M., Fichefet, T., Goosse, H., Bouillon, S., Madec, G., and Maqueda, M. A. M.: Simulating the mass bal-  
574 ance and salinity of Arctic and Antarctic sea ice. 1. Model description and validation, *Ocean Modelling*, 27, 33–53,  
575 <https://doi.org/10.1016/j.ocemod.2008.10.005>, <https://doi.org/10.1016/j.ocemod.2008.10.005>, 2009.
- 576 Winther, N. G. and Johannessen, J. A.: North Sea circulation: Atlantic inflow and its destination, *Journal of Geophysical Research*, 111,  
577 <https://doi.org/10.1029/2005jc003310>, <https://doi.org/10.1029/2005jc003310>, 2006.
- 578 Zalesak, S. T.: Fully multidimensional flux-corrected transport algorithms for fluids, *Journal of Computational Physics*, 31, 335–362,  
579 [https://doi.org/10.1016/0021-9991\(79\)90051-2](https://doi.org/10.1016/0021-9991(79)90051-2), [https://doi.org/10.1016/0021-9991\(79\)90051-2](https://doi.org/10.1016/0021-9991(79)90051-2), 1979.